Ferroelectrics, 1995, Vol. 165, pp. 1–26
Reprints available directly from the publisher
Photocopying permitted by license only

QUANTITATIVE IN-SITU PHOTOPYROELECTRIC SPECTROSCOPY OF OPTOELECTRONIC QUANTUM STRUCTURES. THEORY AND EXPERIMENT WITH $Al_{0.6}Ga_{0.4}As$/GaAs QUANTUM WELLS

ANDREAS MANDELIS and C. ALISON DA SILVA
Photothermal and Optoelectronic Diagnostics Laboratory,
Department of Mechanical Engineering, University of Toronto,
Toronto, Ontario M5S 1A4 Canada

(Received December 10, 1993; in final form January 4, 1994)

Quantitative photopyroelectric (PPE) optical absorption coefficient spectra of an (Al,Ga)As/GaAs multiple quantum well were obtained *in-situ* on the semi-insulating GaAs substrate completely non-intrusively in the region 900–1080 nm and in the presence of significant absorption form the substrate. The two spectra were decoupled numerically by using a rigorous coupled electromagnetic/thermal-wave photopyroelectric model and optical reflectance and transmittance spectra obtained independently from the PPE spectra. The role of thermal contact resistance at the sample-pyroelectric interface was examined and found to be important for quantitative analysis. An iterative numerical technique matching the theory to the data with the quantum well optical absorption coefficient as the variable parameter yielded quantitative spectra with *ca.* 10% experimental uncertainty. Superior PPE resolution of absorption coefficients due to the quantum well superlattice to the purely optical spectroscopies was observed, thus allowing ultra-thin film *in-situ* quantitative spectroscopy in the GaAs sub-bandgap region for the first time.

Keywords: Photopyroelectric, spectroscopy, optoelectronic, photonic, quantum wells, optical absorption coefficient.

I. INTRODUCTION

In recent years there has been an increasing need for fast and reliable techniques for the purpose of determining the optical properties of semiconductor thin films, quantum wells and superlattice heterostructures. One important optical characteristic of an optoelectronic material is its optical absorption coefficient spectrum, $\beta(\lambda)$, which gives important and unique information on the physical processes of the interaction of light with the energetic structure of the material. In quantum wells studying these absorption coefficients in the vicinity of the material band-gap is the most direct way of probing for quantum size effects such as the quantized electronic states within the quantum well, their energy separation (heavy and light holes) and the binding energy of confined excitons. In addition, optical absorption spectra of thin films are of fundamental interest in the development of selectively absorbing layers for the photothermal conversion of solar energy.

Quantum wells and superlattice heterostructures are modern 'engineered' materials that are rapidly finding new applications. One very popular type is the $Al_xGa_{1-x}As$/GaAs multiple quantum well (MQW) grown on a semi-insulating (SI) GaAs substrate. These materials are currently being used for high-speed optical modulation, diode laser mode locking, gates for optical logic, linearized optical

modulators and optical level shifters. The burgeoning study of these structures can largely be attributed to improvements in production techniques, specifically, Molecular Beam Epitaxy (MBE), which is capable of the precise production of multiple layers, of differing material composition and with thicknesses as little as a few Angströms.

Although various purely optical measurement techniques have traditionally been used to determine $\beta(\lambda)$ of thin layers, they become much less accurate for low absorptions. Alternatively then, photothermal techniques must be employed when extended signal dynamic range is required in low absorption regions. These methods offer certain advantages because they measure the 'thermal wave' produced from the absorption of intensity modulated electromagnetic radiation, rather than the purely optical changes in the transmitted and reflected energy.

The present work represents the first photopyroelectric spectroscopic (PPES) investigation of optoelectronic MQW thin layer structures on absorbing substrates. Earlier applications of PPES to electronic and optoelectronic materials spectroscopy have been reported for the determination of optical absorption coefficient spectra, $\beta(\lambda)$, and optical-to-thermal energy conversion (non-radiative) coefficient spectra, $\eta(\lambda)$, of crystalline (c) Ge,[1] as well as those of amorphous silicon thin films on either a quartz[2,3] or on a c-Si substrate.[4]

In this PPES application to MQW structures, the question of calculating the optical absorption spectrum of an (Al,Ga)As/GaAs MQW layer ($\beta_{MQW}(\lambda)$), at photon wavelengths of 900 nm to 1080 nm is addressed. These wavelengths correspond to incident photons that are just below the band-gap energy of GaAs ($\sim$1.4 eV at room temperature), in which regime both the MQW and substrate are moderately optically absorbing. To our knowledge there are no published (Al,Ga)As/GaAs $\beta_{MQW}(\lambda)$ results in this near infrared region with either destructive or non-destructive experimental techniques.

Information on optical absorption spectra of (Al,Ga)As/GaAs quantum wells at room temperature is available for only higher visible photon energies. An overview of the existing spectroscopy is now given. Using transmission spectroscopy, Filipowicz *et al.*[5] studied (Al,Ga)As after partially removing the GaAs substrate in order to allow a reasonable amount of light to penetrate the sample. Thus, the absorption values calculated were an overestimate of β_{MQW} and ranged from approximately 1.5×10^4 cm^{-1} to 2.8×10^4 cm^{-1} for a wavelength range of 842 nm $< \lambda <$ 850 nm. Miller *et al.*[6] completely removed the MQW substrate and cap layer, which introduced some unavoidable etching of the epitaxial layer. Consequently, the β_{MQW} coefficients calculated were said to be underestimated and lay between 3.8×10^3 cm^{-1} and 5.0×10^2 cm^{-1} for the wavelength range of 780 nm to 855 nm.

Penna *et al.*[7] were the first investigators to use a thermal-wave technique (photothermal deflection spectroscopy, PDS) to obtain single quantum well spectra. Yacoubi[8] also used PDS to obtain spectra of (Ga,Al)As and (Ga,As)Sb films on GaAs. Using the two-layer model proposed by Fernelius,[9] this author determined the $\beta(\lambda)$ spectra of these compounds. Penna *et al.* removed the GaAs substrate to avoid the effects of its absorption and obtained qualitative spectra in the range 840–865 nm, structured due to heavy and light exciton absorptions. Yacoubi was only able to determine the substrate and thin-film $\beta(\lambda)$ spectra quantitatively in

different spectral regions, that is, he could not resolve the spectral overlap in regions where both layers absorbed significantly. Among the purely optical techniques, MQW characterization mainly consists of luminescence, absorptance and photoreflectance investigations.[10–13]

II. PHOTOPYROELECTRIC INSTRUMENTATION AND MATERIALS

The PPE spectrometer used in this work has been described elsewhere[14] and is illustrated in Figure 1. This is a real-time normalizing set-up. Physically the spectrometer involves two polyvinylidene fluoride (PVDF) pyroelectric detectors; one is the sample detector on which the specimens are placed and the other is a reference detector. The purpose of the reference detector is to remove the effects of the spectral variations of the incident light on the sample generated PPE voltage, in the course of the experiment. The normalizing calculation is carried out by a computer program which divides the complex (magnitude and phase) sample PPE voltage by the complex reference PPE voltage, resulting in $V_N = V_S/V_R$, and $\theta_D = \theta_S - \theta_R$ where the complex PPE voltage is separated into its magnitude, V, and phase, θ, and the subscripts N, D, S and R refer to the normalized, difference,

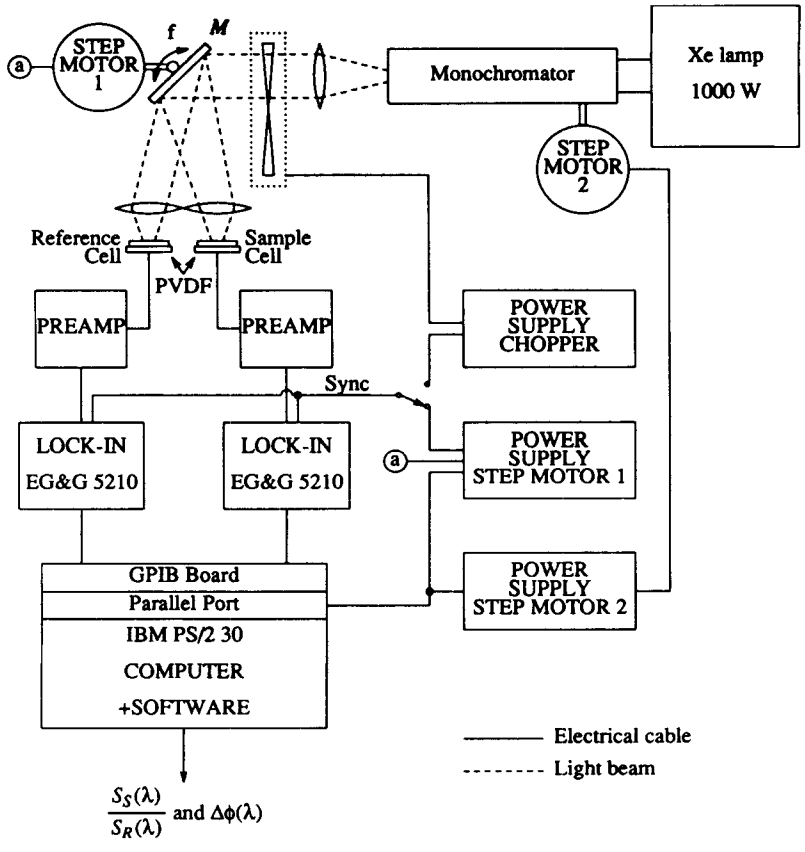

FIGURE 1 Dual-channel PPES instrumentation.

sample and reference PPE signals, respectively. An oscillating mirror was used to direct the monochromatized 1000 W Xe lamp light alternately to the sample and to the reference PVDF detectors.

The spectrometer lens arrangement focused light on both the sample and the reference surfaces. Care was taken for the optical path lengths and the focused spot sizes to be approximately the same. The area illuminated on the sample had to be small enough so that a strong irradiance was maintained, but not too small lest three-dimensional effects might become significant to the theoretical analysis. Since the quantum well samples investigated were *ca.* 500 μm thick, an illumination area of no less than 1×2 mm^2 was used to ensure that a one-dimensional PPES model can be employed.

The front surface of each PPE detector was sprayed with a thin coating of black paint as shown in Figure 2. Consequently, the reflection off of the Al-Ni metallized PVDF[15] was virtually eliminated. This increased the absorbed energy on the detectors significantly and, thereby, increased the photopyroelectric voltage generated. The signal from each of these detectors was then bandpass-filtered by an Ithaco low-noise pre-amplifier (model 1201) before being sent to a EG&G lock-in amplifier (model 5210). Special care had to be taken on account of the long-term drift in the output intensity of the Xe lamp. Over a 24 hour period of continuous lamp operation, spectral drifts of up to 10% in lamp throughput were observed. Therefore, real-time normalization at each recorded wavelength became necessary to eliminate this problem.

(Al,Ga)As/GaAs MQWs on semi-insulating (SI) GaAs substrates were obtained for the purposes of this work.[16] These specimens were roughly 3 mm $\times$ 4 mm in area with only the top, MQW side, polished. Unfortunately, detailed information on the structure of the MQW samples was not available. This was not a great impediment though, since the $\beta_{MQW}(\lambda)$ calculations using the MQW and PPE signal generation model presented in the next section required mainly the total thickness of the stack of quantum wells and the thickness of the substrate layer as physical dimensions. Table I tabulates the known information on the samples.[16]

The (Al,Ga)As/GaAs MQW used extensively in this work were reported[17] to have room temperature LH_1-E_1 and HH_1-E_1 transitions at photon wavelengths of approximately 842 nm and 860 nm respectively. This was supported by the similarly

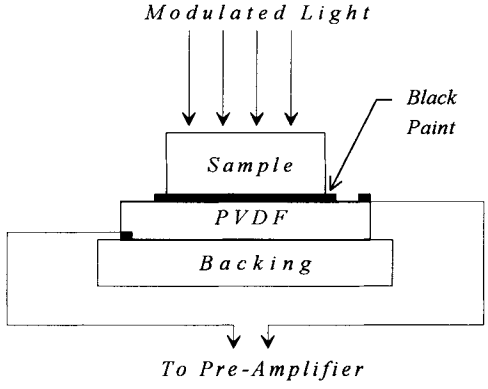

FIGURE 2 Geometric configuration of quantum well sample on the PPE detector.

TABLE I
Fabrication parameters of MQW samples used in PPES investigations

Sample Number	277
Well width	200Å
Barrier width	250Å
No. of periods	25
Mole fraction, x	0.6
Thickness (overall)	514 μm

located LH_1-E_1 and HH_1-E_1 peaks seen in other (Al,Ga)As/GaAs MQWs.[5–7,18] The Pauli Exclusion Principle dictates that when wavefunctions of adjacent quantum wells interact, the energy level becomes 'degenerate.' Light and heavy holes are therefore sub-bands of their original band at that particular quantum number. Light holes, LH, are further away from the band edge than heavy holes, HH, and therefore a LH_1-E_1 transition, where E_1 is the first bound state in the conduction band, takes more energy than a HH_1-E_1 transition.

A specimen of semi-insulating GaAs, of the same type as the MQW substrates, was required in order that the MQW PPE spectra could be distinguished from the substrate spectra. It too was only polished on one side and was measured to be 630 μm thick.

III. PPE SIGNAL GENERATION THEORY FROM MULTILAYERED ABSORBING SOLIDS

A. *The Photopyroelectric Circuit*

Given that thermal diffusion depth in PVDF is approximately 47 μm (at the modulation frequency of 8 Hz used in most of the experimental work) and the thickness of the pyroelectric film is 52 μm, the following lumped circuit analysis can be used to determine the voltage response of PVDF to a modulated incident beam.[19] First, the incident light can be written as,

$$I = I_0 + I_\omega e^{i\omega t} \tag{1}$$

where I_ω is the magnitude of the oscillating component of the incident intensity about an average I_0. The temperature, Θ_p, in the pyroelectric film can then be found by solving the differential equation:

$$\varepsilon I = H\frac{d\Theta_p}{dt} + G\Theta_p \tag{2}$$

where H is the thermal capacity, ε is the emissivity and G is the radiative conductance of the surface of the material. The amplitude of the ac component, Θ_ω, of the excess temperature at angular frequency ω becomes,

$$\Theta_\omega = \varepsilon I_\omega (G^2 + \omega^2 H^2)^{1/2}. \tag{3}$$

The pyroelectric coefficient, p (a constant for homogeneous polarization) then relates the amplitude of the oscillating excess temperature in the pyroelectric to the amplitude of the charge developed across an area, A:

$$|q(\omega)| = pA\Theta_\omega \tag{4}$$

If the pyroelectric element is then represented in the electrical circuit as a capacitance, C_p, and a resistance, R_p, the alternating charge on the electrodes is equivalent to a current generator, i_p where,

$$|i_p(\omega)| = \omega pA\Theta_\omega \tag{5}$$

Then, if the pyroelectric is connected across the input of an amplifier as shown in Figure 3 the voltage applied to the amplifier is found by calculating the voltage across the equivalent circuit impedances. Thus,

$$|V(\omega)| = |i_p(\omega)||Z| = \frac{|i_p|R}{\sqrt{(1 + \omega^2\tau_E^2)}} \tag{6}$$

in which $\tau_E = RC$ is the equivalent circuit time constant. Hence,

$$|V(\omega)| = \frac{\omega pA\Theta_\omega R}{\sqrt{(1 + \omega^2\tau_E^2)}} \tag{7}$$

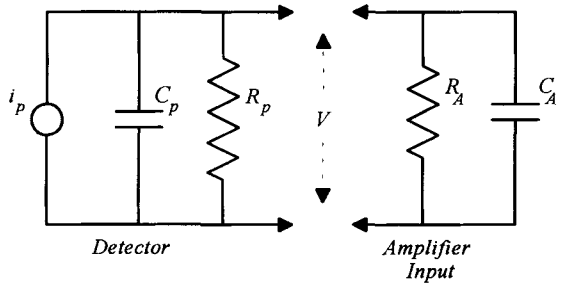

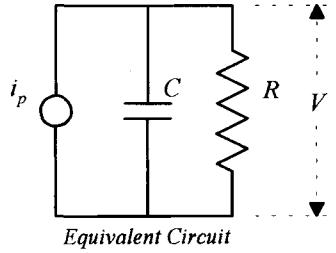

FIGURE 3 Equivalentic circuit of pyroelectric detector and pre-amplifier set-up.

where the amplitude of the pyroelectric voltage is then a simple relation which is directly proportional to the temperature change in the material and its pyroelectric coefficient, p. Equation (7) is rewritten now in its complex form:

$$V(\omega) = \frac{i\omega pA\langle\Theta_p(\omega)\rangle R}{(1 + i\omega\tau_E)} \tag{8}$$

Furthermore, the normalized PPE voltage can be obtained through division of Equation (8) by the reference PPE voltage:

$$V_N(\omega) = \frac{V(\omega, t)}{V_R(\omega, t)} = \frac{\langle\Theta_p(\omega)\rangle}{\langle\Theta_p(\omega)\rangle_R} \tag{9}$$

The normalization process conveniently removes both the effects of the spectral throughput of the Xe lamp light source and of the pyroelectric circuit parameters seen in Equation (8).

From the above equation it is apparent that the average temperatures $\langle\Theta_p(\omega)\rangle$, of the reference and sample PVDF detectors must be found. Then, from the relationship:

$$\langle\Theta_p(\omega)\rangle = \frac{1}{L_p}\int_{L_p}\Theta_p(x, \omega)\,dx \tag{10}$$

it follows that $\Theta_p(x, \omega)$, the temperature distribution of the ac temperature component in the pyroelectric, must first be derived.

B. *The Optical (Electromagnetic) Fields*

Figure 4 illustrates the standing wave patterns set up when electromagnetic radiation impinges on a three-layer sample. Layer (1) refers to the ambient gas (air), while layers (2) and (3) may be any two solid media on top of the substrate, layer (4).

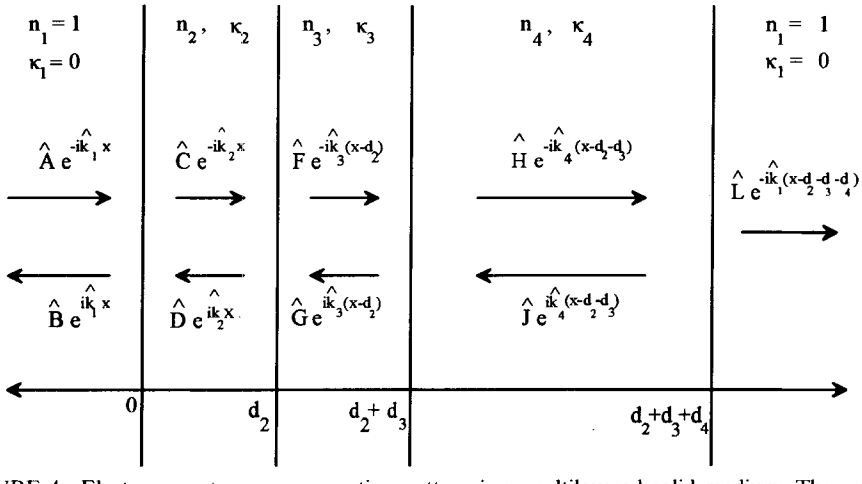

FIGURE 4 Electromagnet wave propagation pattern in a multilayered solid medium. The various symbols are defined in the text.

It should be noted that air is also assumed to be in direct contact with the lower surface of the substrate. In practice, a pyroelectric (detector) layer would be expected in contact with the sample. The reasons for which the optical properties of air were assumed is the experimental fact that in the contact of two imperfect plane surfaces, there will always be a thin layer of air between sample and detector. Furthermore, the black coating on the PVDF element creates a virtually perfect light absorbing surface and thus there is no need to consider light reflecting off of the pyroelectric and returning to the sample. In Figure 4 the following symbols and/or expressions have been defined:

Symbols with a "hat" indicate a complex electric field quantity.

The coefficients $\hat{A}$, $\hat{C}$, $\hat{F}$, $\hat{H}$, and $\hat{L}$ represent the magnitude and phase of the net forwardly transmitted electromagnetic waves; however, $\hat{A}$, the light incident on layer (2), has a phase angle of zero degrees because the air is assumed to be optically non-absorbing. The waves travelling from right to left i.e., $\hat{B}$, $\hat{D}$, $\hat{G}$, and $\hat{J}$ are the net reflected waves. Note that these coefficients are all dependent on the spectral output of the optical source.

$\hat{k}_j(\lambda) \equiv 2\pi/\lambda[n_j(\lambda) - i\kappa_j(\lambda)]$ is the optical field complex wavenumber; n_j and κ_j are the real and imaginary parts of the complex refractive index of layer (j), where all factors k, n and κ are functions of wavelength; and

$$\begin{aligned} \exp[-i\hat{k}_j(\lambda)d_j] &= \exp\left[-i\frac{2\pi}{\lambda}n_j(\lambda)d_j\right]\exp\left[-\frac{2\pi}{\lambda}\kappa_j(\lambda)d_j\right] \\ &= \exp\left[-\frac{i\gamma_j(\lambda)d_j}{2}\right]\exp\left[-\frac{\beta_j(\lambda)d_j}{2}\right] \end{aligned} \tag{11}$$

This introduces the definition of the optical absorption coefficient:

$$\beta_j(\lambda) \equiv \frac{4\pi}{\lambda}\kappa_j(\lambda); \tag{12}$$

and the optical propagation coefficient,

$$\gamma_j(\lambda) \equiv \frac{4\pi}{\lambda}n_j(\lambda) \tag{13}$$

Another two important definitions are the transmission coefficient $\hat{t}_{ij}$, across the interface separating regions i and j,

$$\hat{t}_{ij}(\lambda) \equiv \frac{2\hat{k}_i(\lambda)}{\hat{k}_i(\lambda) + \hat{k}_j(\lambda)} \tag{14a}$$

and the reflection coefficient,

$$\hat{r}_{ij}(\lambda) \equiv \frac{\hat{k}_i(\lambda) - \hat{k}_j(\lambda)}{\hat{k}_i(\lambda) + \hat{k}_j(\lambda)} \tag{14b}$$

The electromagnetic field equations for each layer are comprised of electric and magnetic field equations, Figure 4; for the electric field propagation:

$$\hat{E}_1(x) = \hat{A}e^{-i\hat{k}_1 x} + \hat{B}e^{i\hat{k}_1 x}; \qquad x \leq 0 \tag{15a}$$

$$\hat{E}_2(x) = \hat{C}e^{-i\hat{k}_2 x} + \hat{D}e^{i\hat{k}_2 x}; \qquad 0 \leq x \leq d_2 \tag{15b}$$

$$\hat{E}_3(x) = \hat{F}e^{-i\hat{k}_3(x-d_2)} + \hat{G}e^{i\hat{k}_3(x-d_2)}; \qquad d_2 \leq x \leq d_2 + d_3 \tag{15c}$$

$$\hat{E}_4(x) = \hat{H}e^{-i\hat{k}_4(x-d_2-d_3)} + \hat{J}e^{i\hat{k}_4(x-d_2-d_3)}; \qquad d_2 + d_3 \leq x \leq d_2 + d_3 + d_4 \tag{15d}$$

$$\hat{E}_5(x) = \hat{L}e^{-i\hat{k}_1(x-d_2-d_3-d_4)}; \qquad x \geq d_2 + d_3 + d_4, \tag{15e}$$

The complex field-amplitude coefficients $\hat{A}, \ldots \hat{L}$ remain to be determined from boundary conditions of the electric and magnetic field components in Figure 4. The magnetic field equations are obtained from $H_j = (i/\omega\mu)[\partial E_j(x)/\partial x]$, where $E_j(x)$ is the electric-field in medium (j):

$$\hat{H}_1(x) = \frac{\hat{k}_1}{\omega\mu_1}(\hat{A}e^{-i\hat{k}_1 x} - \hat{B}e^{i\hat{k}_1 x}); \qquad x \leq 0 \tag{16a}$$

$$\hat{H}_2(x) = \frac{\hat{k}_2}{\omega\mu_2}(\hat{C}e^{-i\hat{k}_2 x} - \hat{D}e^{i\hat{k}_2 x}); \qquad 0 \leq x \leq d_2 \tag{16b}$$

$$\hat{H}_3(x) = \frac{\hat{k}_3}{\omega\mu_3}(\hat{F}e^{-i\hat{k}_3(x-d_2)} - \hat{G}e^{i\hat{k}_3(x-d_2)}); \qquad d_2 \leq x \leq d_2 + d_3 \tag{16c}$$

$$\hat{H}_4(x) = \frac{\hat{k}_4}{\omega\mu_4}(\hat{H}e^{-i\hat{k}_4(x-d_2-d_3)} - \hat{J}e^{i\hat{k}_4(x-d_2-d_3)}); \qquad d_2 + d_3 \leq x \leq d_2 + d_3 + d_4 \tag{16d}$$

$$\hat{H}_5(x) = \frac{\hat{k}_1}{\omega\mu_1}\hat{L}e^{-i\hat{k}_1(x-d_2-d_3-d_4)}; \qquad x \geq d_2 + d_3 + d_4 \tag{16e}$$

in which μ_i is the *permeability* of the medium i. From electromagnetic theory, $\mu_i = \mu_r\mu_0$, where μ_0 is the permeability of free space ($=4\pi \times 10^{-7}$ henrys/m), and μ_r is the relative permeability of medium (r). The relative permeabilities of most materials (except ferromagnetic materials) are close to unity; for example, the permeabilities of air and copper are practically the same as that of free space. Thus, the denominator terms in the above equations will all eventually cancel out.

The boundary conditions for Equations (15) and (16) are continuity criteria at the various interfaces, namely: $\hat{E}_i(x) = \hat{E}_j(x)$, for $i = 1$ to 4, $j = 2$ to 5 and $x = 0, d_2, d_2 + d_3, d_2 + d_3 + d_4$ respectively, and similarly for the magnetic terms. Applying the boundary conditions one obtains 8 equations with 9 unknowns. The extra unknown is the magnitude (and phase) of the incident radiation. Nevertheless, since the same radiation is also incident on the reference PPE detector, this term will conveniently cancel out when the sample PPE voltage is normalized.

Using these equations the expression for the fraction of incident light transmitted through the three-layered sample to the PPE detector can be obtained i.e., the coefficient corresponding to the total transmittance, $\hat{T} \equiv \hat{L}/\hat{A}$. However, by making

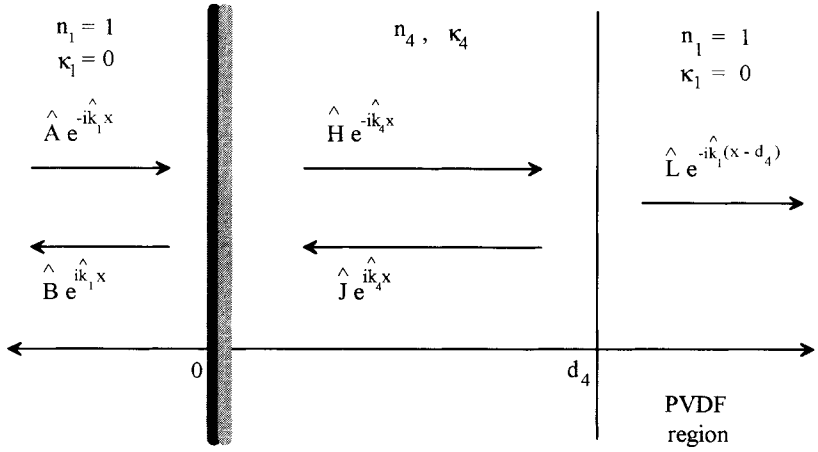

FIGURE 5 Simplified electromagnetic wave propagation pattern in the multilayered solid of Figure 4. The thin layers (2) and (3) have been lumped into a single interface which only affects the transmission and reflection components of the incident radiation.

the following important simplification, the extremely lengthy task of solving for the electric field distributions in all three sample layers may be avoided. Given that the two top layers of the sample are very thin compared to the substrate (recall from Table I: the MQW is 1.15 μm, the buffer 1.0 μm while the SI GaAs substrate is 512 μm thick), there is little advantage to considering the distribution of the optical and thermal waves within these layers. In fact, the thermal energy created in the two top layers may be lumped together to form a heat source on the surface of the substrate layer, Figure 5. As such, it is only necessary to solve for the electric field in the substrate layer.

The complex electric field in the substrate layer is

$$\hat{E}_4(x) = \hat{A}\left(\frac{\hat{T}}{\hat{t}_{41}} e^{i\hat{k}_4 d_4}[e^{i\hat{k}_4(d_2+d_3)} e^{-i\hat{k}_4 x} + \hat{r}_{41} e^{-i\hat{k}_4(2d_4+d_2+d_3)} e^{i\hat{k}_4 x}]\right), \tag{17}$$

where the optical transmission coefficient of the sample is

$$\begin{aligned}\hat{T} = \hat{L}/\hat{A} = {} & \hat{t}_{12}\hat{t}_{23}\hat{t}_{34}\hat{t}_{41} e^{i(\hat{k}_2 d_2 + \hat{k}_3 d_3 + \hat{k}_4 d_4)}\{1 + \hat{r}_{12}\hat{r}_{23} e^{-2i\hat{k}_2 d_2} + \hat{r}_{23}\hat{r}_{34} e^{-2i\hat{k}_3 d_3} \\ & + \hat{r}_{34}\hat{r}_{41} e^{-2i\hat{k}_4 d_4} + \hat{r}_{12}\hat{r}_{41} e^{-2i(\hat{k}_2 d_2 + \hat{k}_3 d_3 + \hat{k}_4 d_4)} + \hat{r}_{23}\hat{r}_{41} e^{-2i(\hat{k}_3 d_3 + \hat{k}_4 d_4)} \\ & + \hat{r}_{12}\hat{r}_{34} e^{-2i(\hat{k}_2 d_2 + \hat{k}_3 d_3)} + \hat{r}_{12}\hat{r}_{23}\hat{r}_{34}\hat{r}_{41} e^{-2i(\hat{k}_2 d_2 + \hat{k}_4 d_4)}\}\end{aligned} \tag{18}$$

Since, in the simplified model it is easier to write and solve the thermal equations using the dimensions 0 to d_4 instead of $(d_2 + d_3)$ to $(d_4 + d_2 + d_3)$, Equation (17) is rewritten as:

$$\hat{E}_4(x) = \hat{A}\left(\frac{\hat{T}}{\hat{t}_{41}} e^{i\hat{k}_4 d_4}[e^{-i\hat{k}_4 x} + \hat{r}_{41} e^{-i\hat{k}_4(2d_4 - x)}]\right) \tag{19}$$

The optical transmittance of the simplified sample model must clearly be the same as for the full sample model since it still expresses the amount of electromagnetic radiation transmitted through the entire system.

The heat sources due to the thin absorbing films on top of the SI GaAs substrate

are calculated using the well known energy equation $A_i = 1 - T_i - R_i$, where A_i is the absorptance of layer i; T_i is the transmittance through the layer; and R_i is the reflectance. It must be remembered, however, that the absorbed energy in a particular layer must be multiplied by the nonradiative quantum efficiency of that layer in order to obtain the nonradiative or thermal energy. A_2 and A_3, the coefficients of the thermal energy created within the two thin top layers of the sample, are calculated using the appropriate transmission and reflection coefficients (Appendix).

The distributed thermal source in the substrate layer (4) can be obtained by noting that the form of $\hat{A}_4(x)$, the complex field of the absorbed optical energy, follows the same behavior as the attenuating electric field, $\hat{E}_4(x)$. Hence,

$$\hat{A}_4(x) = \hat{A}(A_{4m}[e^{-i\hat{k}_4 x} + \hat{r}_{41}e^{-i\hat{k}_4(2d_4 - x)}]) \tag{20}$$

where A_{4m} is a constant solved for below. Electromagnetic theory states that the energy of an electromagnetic field is equal to half the electric field times its complex conjugate. Thus,

$$\frac{I_\omega}{2}|\hat{A}_4(x)|^2 = \frac{I_\omega}{2}(A_{4m}^2[e^{-\beta_4 x} + |\hat{r}_{41}|e^{-\beta_4(2d_4 - x)} + 2|\hat{r}_{41}|e^{-\beta_4 d_4}\cos(\gamma_4(d_4 - x) - \theta_{41})]) \tag{21}$$

where θ_{41} is the phase change that occurs when light is reflected off the (4/1) interface. I_ω encountered in Equation (1) is defined as:

$$I_\omega \equiv \hat{A}\hat{A}^* = |\hat{A}|^2 \tag{22}$$

The total absorbed energy in layer (4), is equal to:

$$\frac{I_\omega}{2}\int_0^{d_4}|\hat{A}_4(x)|^2\,dx = \frac{I_\omega}{2}A_4 = \frac{I_\omega}{2}(1 - T_4 - R_4) \tag{23}$$

where T_4 and R_4 are the transmittance and reflectance of layer (4) and $A_4 = |\hat{A}_4|^2$. Then,

$$A_4 = A_{4m}^2\int_0^{d_4}[e^{-\beta_4 x} + |r_{41}|^2 e^{-\beta_4(2d_4 - x)} + 2|r_{41}|e^{-\beta_4 d_4}\cos(\gamma_4(d_4 - x) - \theta_{41})]\,dx \tag{24}$$

Hence,

$$A_{4m}^2 = \frac{\beta_4 A_4}{[1 - e^{-\beta_4 d_4} + |\hat{r}_{41}|^2 e^{-\beta_4 d_4} - |\hat{r}_{41}|^2 e^{-2\beta_4 d_4}]} \tag{25}$$

where the trigonometric term has been averaged out.

A_4, the fraction of the incident energy which is absorbed in the substrate layer, was obtained from the expression (A.1), in the Appendix

$$A_4 = |\hat{T}_{14}|^2(1 - |\hat{R}_{31}|^2 - |\hat{T}_{31}|^2) \tag{26}$$

where $|\hat{T}_{14}|^2$ is the fraction of energy transmitted through the front air (layer 1) to the substrate (layer 4), and is equal to:

$$|\hat{T}_{14}|^2 = \left| \frac{\hat{t}_{12}\hat{T}_{24}e^{-i\hat{k}_2 d_2}}{1 + \hat{r}_{12}\hat{R}_{24}e^{-2i\hat{k}_2 d_2}} \right|^2 \tag{27}$$

Also, in Equation (26) $|\hat{R}_{31}|^2$ is the total reflectance from layer (4), while $|\hat{T}_{31}|^2$ is the total transmittance to layer (4). These are written in terms of their field reflection and transmission coefficients, Equations (A.10). Similarly, in Equation (27) the terms $|\hat{R}_{24}|^2$ and $|\hat{T}_{24}|^2$ are the total reflectance and transmittance involving layers (2) to (4) and are given by Equations (A.3).

C. *The Thermal-Wave Fields*

Once the heat sources on the surface and within the substrate material are known, (see Appendix), the system of thermal-wave equations leading to the signal in the PPE detector can be considered. From the schematic diagram, Figure 5, it follows that the coupled equations of the thermal-wave system must include expressions for the thermal-wave in air, thin absorbing films, SI-GaAs and pyroelectric detector. Note that the use of the simplified model of Figure 5 reduces the number of thermal-wave equations by two. However, a fourth equation may be necessary if the thermal energy leaking into the metal backing of the PVDF housing is significant. The decision on whether to introduce this layer depends on how thermally thick the pyroelectric is. To be truly thermally thick the modulation frequency must be such that the condition

$$f >> f_c \equiv \frac{\alpha_p}{\pi L_p^2} \tag{28}$$

is satisfied.[21] The critical frequency, f_c, for PVDF is equal to 5 Hz for the 52 μm thick film used in our experiments. While the 8 Hz modulation frequency used in most of the experiments meant that the PVDF was not completely thermally thick, it represented a compromise between the strength of the thermal signal received by the PPE detector, and true thermal thickness of this layer. The small magnitude of the PPE voltage with the MQW sample in place in the opaque region, compared to the reference voltage at the same wavelengths (a difference of *ca.* two orders of magnitude) led to the reasonable conclusion that thermal energy diffusion into the backing might only be significant for the reference photopyroelectric sensor. Therefore, the PPE PVDF detector was assumed to be semi-infinite in the sample thermal-wave theoretical model but of infinite thickness in the reference theoretical model.

Hence, the coupled thermal-wave equations for the simplified mutilayer model can now be formulated for the geometry of Figure 5:

$$\frac{d^2\Theta_1(x, \omega)}{dx^2} - \sigma_1^2\Theta_1(x, \omega) = 0; \qquad x \leq 0 \tag{29a}$$

$$\frac{d^2\Theta_4(x, \omega)}{dx^2} - \sigma_4^2\Theta_4(x, \omega) = -\frac{I_\omega \eta_4}{2\Lambda_4}|\hat{A}_4(x)|^2; \qquad 0 \leq x \leq d_4 \tag{29b}$$

$$\frac{d^2\Theta_p(x, \omega)}{dx^2} - \sigma_p^2\Theta_p(x, \omega) = 0; \qquad x \geq d_4 \tag{29c}$$

where, it is recalled that the subscripts 1, 4 and p refer to the air above the sample, the substrate layer and the pyroelectric material respectively. Λ_4 is the thermal conductivity of layer (4), and

$$\sigma \equiv (1 + i)\alpha_j \equiv (1 + i)\sqrt{\frac{\omega}{2\alpha_j}} \tag{30}$$

in which α_j is the thermal diffusivity of material (j). The solutions to the above thermal equations are:

$$\Theta_1(x, \omega) = C_1 e^{\sigma_1 x}; \qquad x \leq 0 \tag{31a}$$

$$\Theta_4(x, \omega) = C_2 e^{\sigma_4 x} + C_3 e^{-\sigma_4 x} + \frac{I_\omega \eta_4 A_{4m}^2}{2\Lambda_4}\left\{\frac{e^{-\beta_4 x}}{\sigma_4^2 - \beta_4^2} + |\hat{r}_{41}|^2\left(\frac{e^{-\beta_4(2d_4 - x)}}{\sigma_4^2 - \beta_4^2}\right)\right.$$
$$\left. - 2|\hat{r}_{41}|\left(\frac{e^{-\beta_4 d_4}}{\sigma_4^2 + \gamma_4^2}\right)\cos[\gamma_4(d_4 - x) - \theta_{41}]\right\}; \qquad 0 \leq x \leq d_4 \tag{31b}$$

and

$$\Theta_p(x, \omega) = C_4 e^{-\sigma_p(x - d_4)}; \qquad x \geq d_4 \tag{31c}$$

These solutions are subject to the following boundary conditions:

$$\Theta_1(0, \omega) = \Theta_4(0, \omega) \tag{32a}$$

$$-\Lambda_4 \left.\frac{d\Theta_4(x, \omega)}{dx}\right|_{x=0} + \Lambda_1 \left.\frac{d\Theta_1(x, \omega)}{dx}\right|_{x=0} = \frac{I_\omega}{2}|\hat{S}|^2 \tag{32b}$$

$$-\Lambda_4 \left.\frac{d\Theta_4(x, \omega)}{dx}\right|_{x=d_4} = \frac{1}{R_1}[\Theta_4(d_4, \omega) - \Theta_i] \tag{32c}$$

$$-\Lambda_4 \left.\frac{d\Theta_p(x, \omega)}{dx}\right|_{x=d_4} = \frac{1}{R_2}[\Theta_i - \Theta_p(d_4, \omega)] \tag{32d}$$

and

$$-\Lambda_p \left.\frac{d\Theta_p(x, \omega)}{dx}\right|_{x=d_4} + \Lambda_4 \left.\frac{d\Theta_4(x, \omega)}{dx}\right|_{x=d_4} = \frac{I_\omega}{2}|\hat{T}|^2 \tag{32e}$$

where $|\hat{S}|^2 = (\eta_2 A_2) + (\eta_3 A_3)$, is the lumped heat source on the surface of the substrate, η_2 and η_3 being the non-radiative quantum efficiencies of the thin layers (2) and (3). The other parameters (discussed below) are R_1 and R_2, the thermal resistances of the air gap and black paint respectively, and Θ_i, the temperature of the front surface of the black paint.

The modelling of the thermal resistances was a critical part of this model because their omission resulted in a poor fit of the theory to the experimental data. The arrangement of resistances which best models the physical situation and consequently, gave the best results was that shown in Figure 6. The film of air between the back surface of the sample and the front surface of the black paint creates a temperature discontinuity between the two surfaces which is modeled by the ther-

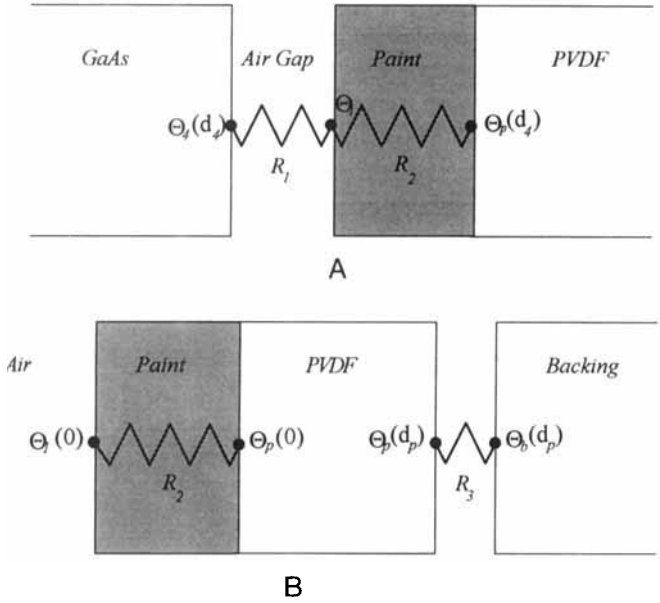

FIGURE 6 Thermal-resistance model of the sample-pyroelectric detector interface. (a): semi-infinite PVDF layer (sample geometry); (b) thermally thin pyroelectric (reference geometry).

mal contact resistance, R_1. A second resistance, R_2 was used to model the effect of the PVDF's black coating on the thermal wave. Since the paint was optically very opaque, it follows that virtually all the light which penetrated the sample was absorbed within a small fraction of the paint depth (the paint had a measured thickness of *ca.* 15 μm). Thus, the amplitude of the ac temperature on the surface of the paint, $|\Theta_i|$, was greater than the amplitude at the back of the point layer. The thermal properties of the paint (diffusivity and conductivity) could not be determined reliably from literature sources; therefore, instead of a fourth thermal-wave equation to represent this layer, R_2 was used to model the temperature discontinuity across the paint. Then assuming that the paint was in intimate contact with the PVDF it follows that the amplitude of the ac temperature at the back surface of the paint is equal to $|\Theta_p(d_4\omega)|$. A simplifying effect of the paint layer is that the PVDF signal generation mechanism is strictly thermal and subsequently, the nonradiative quantum efficiency of the pyroelectric never enters the equations.

Applying the boundary conditions (32) to Equations (31), and solving for C_4 yields, after considerable algebra:

$$C_4 = \left\{\left(\left[\Lambda_4\sigma_4 \sinh(\sigma_4 d_4) + \frac{\cosh(\sigma_4 d_4)}{R_1}\right]\frac{I_\omega|\hat{T}|^2}{2\Lambda_4\sigma_4}\right) + \frac{\Psi\rho_4}{R_1} + \frac{I_\omega|\hat{S}|^2}{2R_1\Lambda_4\sigma_4} - \frac{\Omega\rho_4\cosh(\sigma_4 d_4)}{R_1} + \frac{X\sinh(\sigma_4 d_4)}{R_1} - \frac{b_{14}\Phi}{R_1}\right\} \Bigg/ \left[\frac{b_{p4}\cosh(\sigma_4 d_4)}{R_1} + \left(\frac{R_2\Lambda_p\sigma_p + 1}{R_1} + b_{p4}\Lambda_4\sigma_4\right)\sinh(\sigma_4 d_4)\right]\Bigg\} \tag{33}$$

where

$$\Phi \equiv Q_1' + Q_2' + Q_3' \cos(\delta) \tag{34a}$$

$$\Psi\beta_4 \equiv -Q_1'\beta_4 + Q_2'\beta_4 - Q_3'\gamma_4 \sin(\delta) \tag{34b}$$

$$X \equiv Q_1' e^{-\beta_4 d_4} + Q_2' e^{\beta_4 d_4} + Q_3' \cos(\theta_{41}) \tag{34c}$$

$$\Omega\beta_4 \equiv -Q_1'\beta_4 e^{-\beta_4 d_4} + Q_2'\beta_4 e^{\beta_4 d_4} - Q_3'\gamma_4 \sin(\theta_4). \tag{34d}$$

The following definitions have also been made:

$$Q_i' \equiv \frac{I_\omega \eta_4 A_{4m}^2}{2\Lambda_4} Q_i; \qquad i = 1, 2, 3; \qquad \text{where} \qquad Q_1 \equiv \frac{1}{\sigma_4^2 - \beta_4^2};$$

$$Q_2 \equiv |\hat{r}_{41}|^2 \frac{e^{-2\beta_4 d_4}}{\sigma_4^2 - \beta_4^2}; \qquad Q_3 \equiv 2|\hat{r}_{41}| \frac{e^{-\beta_4 d_4}}{\sigma_4^2 + \gamma_4^2}; \qquad \delta \equiv \gamma_4 d_4 - \theta_{42}. \tag{35a}$$

Also:

$$\rho_i \equiv \frac{\beta_i}{\sigma_i}; \qquad b_{ij} \equiv \frac{\Lambda_i \sigma_i}{\Lambda_j \sigma_j} = \frac{\Lambda_i}{\Lambda_j} \sqrt{\frac{\alpha_j}{\alpha_i}}. \tag{35b}$$

Finally, the average temperature in the photopyroelectric element is:

$$\langle \Theta_p(\omega) \rangle = \frac{1}{d_p} \int_0^{d_p} C_4 e^{-\sigma_p x} \, dx = \frac{C_4}{\sigma_p d_p} (1 - e^{-\sigma_p d_p}) \tag{36}$$

where, as previously discussed, the integral must be from 0 to infinity in the thermally thick mode. Nevertheless, the average temperature is calculated by dividing by the actual PVDF thickness, d_p.

In the thermal-wave model of the reference photopyroelectric detector all the incident radiation is assumed to be absorbed at the front surface of the PVDF black coating. The same thermal resistance, R_2, Figure 6a then models the decrease in temperature from the maximum at the front surface of the paint, $\Theta_1(0)$ to the front surface of the PVDF, $\Theta_p(0)$. For reasons given above, this reference PPE theoretical model also includes the PVDF backing material (stainless steel); in addition, imperfect contact between the pyroelectric and backing was expressed as the thermal contact resistance, R_3, Figure 6b.

The thermal-wave equations for the reference detector geometry are

$$\frac{d^2\Theta_1}{dx^2} - \sigma_1^2 \Theta_1(x, \omega) = 0; \qquad x \le 0, \tag{37a}$$

$$\frac{d^2\Theta_p(x, \omega)}{dx^2} - \sigma_p^2 \Theta_p(x, \omega) = 0; \qquad 0 \le x \le d_p, \tag{37b}$$

and

$$\frac{d^2\Theta_b(x, \omega)}{dx^2} - \sigma_b^2 \Theta_b(x, \omega) = 0; \qquad x \ge d_p. \tag{37c}$$

with solutions:

$$\Theta_1(x, \omega) = C_1 e^{\sigma_1 x}; \qquad x \le 0 \tag{38a}$$

$$\Theta_p(x, \omega) = C_2 e^{\sigma_p x} + C_3 e^{-\sigma_p x}; \qquad 0 \le x \le d_p \tag{38b}$$

$$\Theta_b(x, \omega) = C_4 e^{-\sigma_b (x - d_p)}; \qquad x \ge d_p \tag{38c}$$

These solutions are subject to the boundary conditions:

$$-\Lambda_p \left.\frac{d\Theta_p(x)}{dx}\right|_{x=0} + \Lambda_1 \left.\frac{d\Theta_1(x)}{dx}\right|_{x=0} = \frac{I_\omega}{2} \tag{39a}$$

$$-\Lambda_p \left.\frac{d\Theta_p(x,\omega)}{dx}\right|_{x=0} = \frac{1}{R_2}\left[\Theta_1(0,\omega) - \Theta_p(0,\omega)\right] \tag{39b}$$

$$-\Lambda_p \left.\frac{d\Theta_p(x,\omega)}{dx}\right|_{x=d_p} = -\Lambda_b \left.\frac{d\Theta_b(x,\omega)}{dx}\right|_{x=d_p} \tag{39c}$$

and

$$-\Lambda_p \left.\frac{d\Theta_p(x,\omega)}{dx}\right|_{x=d_p} = \frac{1}{R_3}\left[\Theta_p(d_p,\omega) - \Theta_b(d_p,\omega)\right] \tag{39d}$$

Solving for C_2 and C_3 in $\Theta_p(x,\omega)_R$ gives the expression:

$$\Theta_p(x,\omega)_R = \frac{I_\omega}{2\Lambda_p\sigma_p}\left(\frac{g_2 e^{\sigma_p x} + g_1 e^{-\sigma_p x}}{f_1 g_1 - f_2 g_2}\right) \tag{40a}$$

where

$$g_1 \equiv \left(\Lambda_p\sigma_p + \frac{1}{R_3} + \frac{1}{b_{bp}R_3}\right)e^{\sigma_p d_p}; \quad g_2 \equiv \left(\Lambda_p\sigma_p - \frac{1}{R_3} + \frac{1}{b_{bp}R_3}\right)e^{-\sigma_p d_p}; \tag{40b}$$

$$f_1 \equiv 1 + R_2\Lambda_1\sigma_1 + b_{1p}; \qquad f_2 \equiv 1 + R_2\Lambda_1\sigma_1 - b_{1p}. \tag{40c}$$

The average temperature in the reference pyroelectric is then

$$\langle\Theta_p(x,\omega)\rangle_R = \frac{I_\omega}{2\Lambda_p\sigma_p d_p}\left(\frac{g_2(e^{\sigma_p d_p} - 1) + g_1(1 - e^{-\sigma_p d_p})}{f_1 g_1 - f_2 g_2}\right) \tag{41}$$

Then, as in Equation (9), the normalized PPE voltage is given by Equation (36) divided by Equation (41).

D. Sample Thermal Diffusivity Calculation

Upon simplification of the expression for V_N, Equation (9), which amounts to a simplification of Equation (36) via Equation (33), a separate calculation of the solid substrate (SI-GaAs) thermal diffusivity, α_s, could be made. To obtain the relevant experimental data, a thermal diffusivity experiment was carried out at a single photon energy, in the sample's opaque region; hence, $\beta_4 d_4 >> 1$ and all terms with $\exp(-\beta_4 d_4)$ can be eliminated, from Equation (33). Secondly, the sample is assumed to be thermally thick i.e., $|\sigma_4 d_4| >> 1$. The expression for the reference PPE voltage, Equation (41), can then be simplified if the detector is assumed to be thermally thick. While this assumption is not entirely true for a 52 μm thick PVDF film, yet no significant effect on the diffusivity calculation was found.

Under these conditions, the expression for V_N reduces to:

$$V_N \cong \frac{2b_{p4}A_4|e^{-\sigma_4 d_4}|}{|b_{p4} + R_2\Lambda_p\sigma_p + R_1\Lambda_p\sigma_p|} \tag{42}$$

IV. EXPERIMENTAL AND RESULTS

The MQW which was used as our primary specimen had parameters shown in Table I. The sample was calculated to have a 1.15 μm-thick MQW layer on a 513 μm-thick SI-GaAs substrate. In view of the fact that the foregoing theoretical model in Section III allows for the inclusion of two thin layers on top of the substrate materials, the 1 μm thick buffer layer of pure, amorphous GaAs between the MQW layer and the substrate may be included in the theoretical simulations of the sample and the generated PPE signal. The effect of this layer is small however, since its optical absorption properties are the same as those of SI-GaAs except for slight differences in the 954 nm $< \lambda <$ 1770 nm range[22] owing the fact that the EL2 donor layer was not present.

A. *SI-GaAs PPES*

Figure 7 shows amplitudes and phases of two PPE spectra taken using the same SI GaAs sample. Runs 1 and 2 are slightly shifted relative to each other. As discussed earlier this is due to long-term signal drift, which was thus estimated to introduce a maximum of 10% (amplitude) and 4° (phase) overall uncertainty to the PPE spectra. Generally, however, the spectra are very similar in shape and have nearly the same V_N (1080 nm)/V_N (680 nm) ratio and θ_D (1080 nm) − θ_D (680 nm) difference. In addition, the 90% confidence bars calculated at each point proved to be negligibly small on the above scale. Thus, these PPE spectra were judged to be consistent and reproducible.

No excitonic or interference effects were expected at room temperature in the 680 nm $< \lambda <$ 900 nm opaque region of the PPE spectra for SI GaAs[23] and none were found photopyroelectrically.

B. *MQW PPES*

To accentuate the differences observed between the photopyroelectric MQW spectra and those obtained from SI-GaAs, both sets of curves are displayed in Figure 8. Only the sub-bandgap range 900–1100 nm is shown, because in that region the spectra exhibit the largest variations. Figure 8 is typical of quantum wells on the surface of an absorbing substrate. In the opaque super-bandgap region, theoretical calculations[16] predicted excitonic peaks at room temperature at energies corresponding to 715 nm, 756 nm, and 790 nm, and 811 nm for the particular MQW of Table I. Figure 9 shows the average of three spectral runs, including the 10% uncertainty envelope, as determined from the long-term drift PPE spectra of Figure 7a. Little correlation with the expected theoretical dips in the photopyroelectric

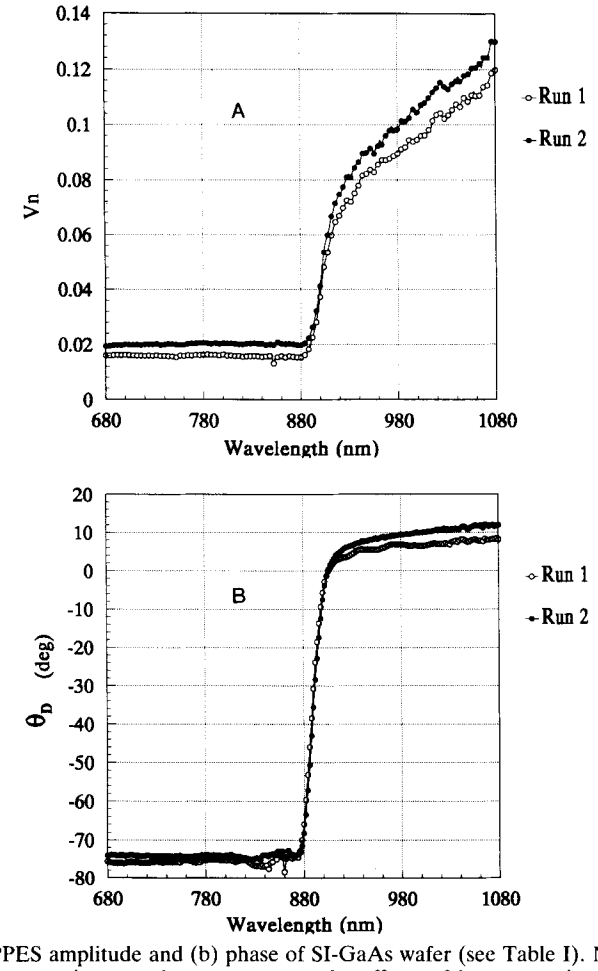

FIGURE 7 (a) PPES amplitude and (b) phase of SI-GaAs wafer (see Table I). Normalized data are shown from two consecutive experiments to assess the effects of long-term signal drift. Modulation frequency: 8 Hz.

spectrum is seen in Figure 9, but the averaged spectra were found to anti-correlate with optical reflectance spectra obtained independently. It was, therefore, concluded that the signal-to-noise ratio (SNR) of the PPE signal in the optically opaque region was not adequate to reveal (perhaps very weak) excitonic structures. For that matter, reflectance spectroscopy also proved unable to verify or negate the theoretical predictions.[16] The anti-correlation trends in the two types of spectra were attributed to optical interference effects. The (Al,Ga)As/GaAs interface has a reflection coefficient of about 0.02. Therefore, multiple reflections either within an optically transparent (Al,Ga)As barrier layer or especially in an absorbing GaAs quantum well layer cannot be the cause of significant interference patterns.[24]

Using the optical theory developed in Section III, a calculation was performed which took into account multiple reflections from the first five interfaces with intermediary layers consisting of GaAs and (Al,Ga)As alternatively, starting with GaAs on top. No interference effects were predicted through modelling the layer

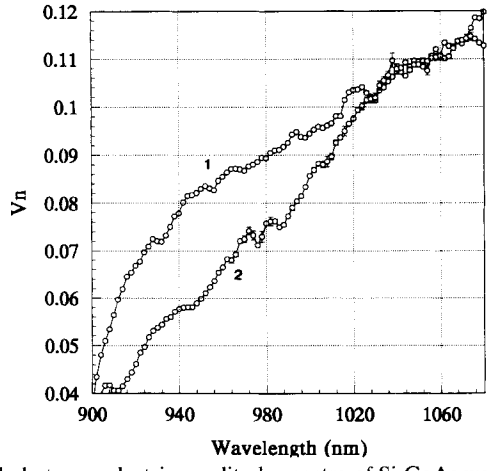

FIGURE 8 Normalized photopyroelectric amplitude spectra of Si-GaAs wafer (#1) and of MQW on Si-GaAs substrate (see Table I) (#2).

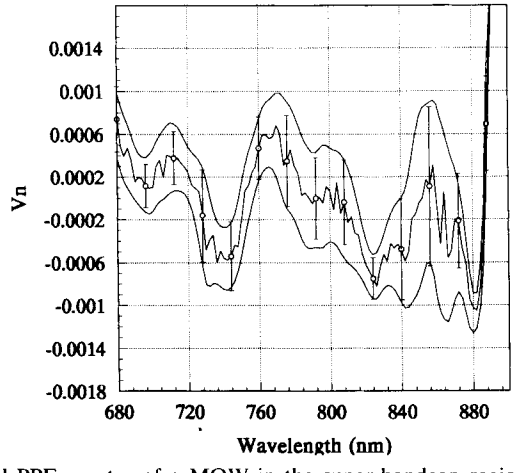

FIGURE 9 Averaged PPE spectra of a MQW in the super-bandgap region of SI-GaAs. Standard deviations and the 10% uncertainty envelope are drawn.

TABLE II

Reflection coefficients from $Al_{0.6}Ga_{0.4}As$-air and GaAs-air interfaces

Material of Top Layer	Air/Top Layer Interface Reflectance
$Al_{0.6}Ga_{0.4}As$	0.30
GaAs	0.34

thicknesses of the MQW (i.e. 200 Å GaAs and 250 Å $Al_xGa_{1-x}As$). Nevertheless, when the 1 μm-thick layer of a buffer (Al,Ga)As was introduced as the second layer, a pronounced interference effect was obtained. This latter spectrum exhibited peaks and dips in approximately the same locations as did the reflectance experiment; furthermore, the change in its reflectance from minimum to maximum was virtually the same as that obtained experimentally. Clearly then, a buffer layer of (Al,Ga)As must be present above the MQW layer in the sample of Table I; this buffer layer is commonly reported by some investigators.[25] Also, the GaAs cap layer is necessary because an (Al,Ga)As/air interface would result in too low a surface reflectance as seen in Table II.

FTIR transmission spectra of the SI-GaAs and the MQW under investigation were also obtained[26] in the 910–2600 nm region. Although the differences observed in Figure 8 could not be easily identified, the GaAs wafer transmission continued to rise monotonically even at wavelengths as large as 2.6 μm. Thus it can be concluded that the SI-GaAs substrate was far from being transparent in the so-called 'optically transparent' range of the PPE experiments (up to 1080 nm). These results then support the gradual slope of the absorption edge seen in both the SI-GaAs and MQW spectra obtained photopyroelectrically, while verifying the unique sensitivity of PPEs in easily resolving spectral variations in the sub-bandgap region of GaAs.

C. *Optical Absorption Coefficient Spectra*

The calculations of $\beta_{MQW}(\lambda)$ were made assuming that optical interference effects, although important in the super-bandgap region, were negligible in the sub-bandgap region. This assumption was supported *a posteriori* by obtaining an estimate of the maximum error in $\beta_{MQW}(\lambda)$ values. FTIR reflectance and transmittance spectra were used as inputs to the model of Section III. Moreover, it must be emphasized

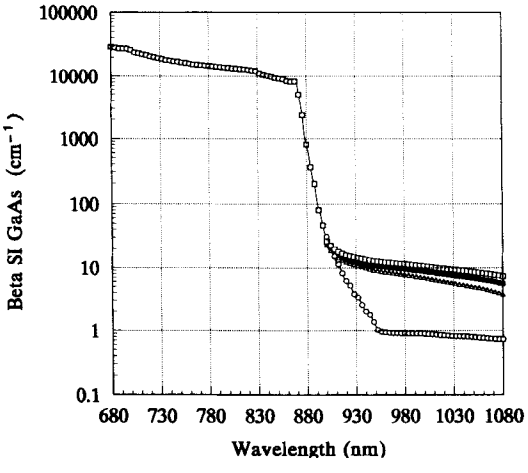

FIGURE 10 Optical absorption spectrum of SI-GaAs. PPE spectroscopic data from Figure 7 were used with thermal resistance values R_1, R_2, R_3, respectively (MKS units): (–△–△–△–) 2.4, 1.86, 2.0 (I); (–●–●–●–) 2.7, 1.6, 2.0 (II); (–□–□–□–) 3.0, 1.31, 2.0 (III); The fourth curve (–○–○–○–) is a SI-GaAs spectrum reconstructed from literature values.[27] Modulation frequency: 8 Hz.

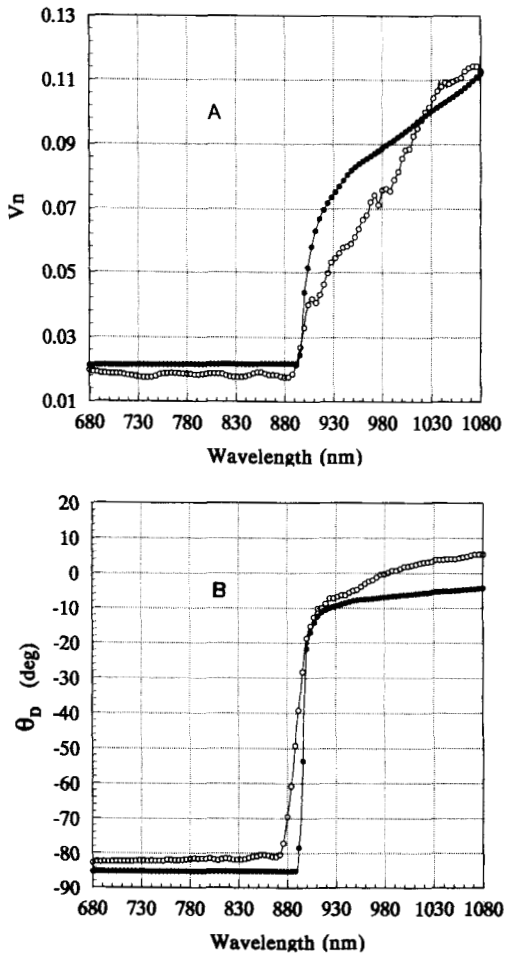

FIGURE 11 Experimental (–○–○–○–) and theoretical (–●–●–●–) PPE spectra of the MQW of Table I using the SI-GaAs spectrum obtained from calculation II in Figure 10. (a) amplitude; (b) phase. Modulation frequency: 8 Hz.

that, since $\beta_{SI\,GaAs}(\lambda)$ and $\beta_{MQW}(\lambda)$ absorption coefficients were calculated such that they produced a MQW PPE spectrum that exactly matched the experiment, the A, R and T values produced with these coefficients are as reliable as can be obtained from the current three-layered model. The optical absorption, $\beta_{SI\ GaAs}(\lambda)$, of the SI-GaAs substrate was first calculated. The initial theoretical PPE spectrum of the SI-GaAs single-layered sample was obtained from imputing the literature values for $\beta_{SI\ GaAs}(\lambda)$, the thermal diffusivity and conductivity, the experimental modulation frequency and the thermal contact resistances R_1, R_2 and R_3. It was found through computer simulations of our theoretical thermal-wave model that R_1, the thermal contact resistance between the sample and the pyroelectric detector, affects the V_N (1080 nm)/V_N (680 nm) ratio of the simulated PPE spectra. R_2, the thermal resistance caused by the layer of black paint, shifts the PPE results vertically, but R_3 has negligible influence. The two resistances, R_1 and R_2, can be estimated by finding the values which give the best match between the theoretical

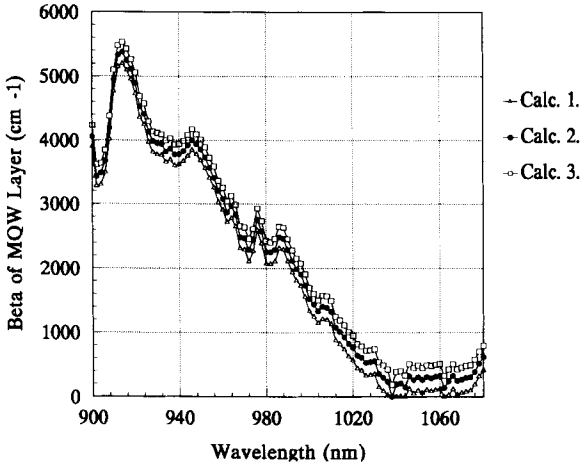

FIGURE 12 Iteratively calculated $Ga_{0.4}Al_{0.6}As$ MQW spectrum from PPE amplitude and phase data and R_j values as per Figure 10. Modulation frequency: 8 Hz.

and experimental PPE spectra (i.e., matching their overall features namely, V_N (1080 nm)/V_N (680 nm) and θ_D (1080 nm) $-$ θ_D (680 nm)). Then $\beta_{SI\ GaAs}(\lambda)$ was calculated by taking the difference in normalized magnitude, V_N, between the experimental PPE and the theoretically obtained (i.e., simulated) spectra, and iteratively adjusting the $\beta(\lambda)$ values of the theoretical curve until this difference was insignificant. Naturally, the thermal resistance parameters used to calculate the original theoretical curve were reused for all subsequent calculations involving a particular sample. Figure 10 shows optical absorption coefficient spectra obtained by use of three different sets of thermal resistance values, consistent with the uncertainty spread in the PPE data. Also shown is a spectrum obtained from the literature.[27] As expected, the absorption coefficient of SI-GaAs in the range 880–1080 nm was found to be somewhat larger than the published values. This is consistent with the FTIR results and reflects the variety of sub-bandgap absorption mechanisms operating in GaAs crystals grown under different conditions. Several literature examples of variations in sub-bandgap absorptions can be found elsewhere.[28] Figure 10 shows, however, that thermal resistance $R_j, j = 1 - 3$, variations consistent with the PPES amplitude and phase experimental data affect the values of the resulting SI-GaAs spectra only moderately. Therefore, these spectra were considered to be quantitative. Further tests matching theoretically the experimental PPE data from various modulation frequencies while keeping R_j constant, yielded satisfactory best fits of both amplitudes and phases at 8 and 16 Hz for the set of R_j parameters indicated by black dots in Figure 10, thus providing further confidence in the dependability of those values. Each of the $\beta_{SI\ GaAs}(\lambda)$ outputs in Figure 10 was used as the substrate optical absorption data for the calculation of simulated MQW spectra. Simulations I, II and III of a MQW sample used the same R_1, R_2 and R_3 as those previously shown in the caption of Figure 10 and employed the $\beta_{SI\,GaAs}(\lambda)$ data obtained at each of these simulations respectively. The simulated spectra thus obtained matched extremely well the V_N (1080 nm)/V_N (680 nm) and θ_D (1080 nm) $-$ θ_D (680 nm) values of the actual MQW experiment, while intermediate values gave only fair matches, Figure 11. Only Simulation II is shown in

this diagram because, as discussed in the foregoing, this set of R_j values matched the experimental frequency-dependent data optimally. All the remaining $\beta_{MQW}(\lambda)$ values were then adjusted until the theoretical curve became an exact match of the experimentally obtained PPE spectrum. The results of the procedure are shown in Figure 12. In this figure, the three slightly shifted $\beta_{MQW}(\lambda)$ curves correspond to the three SI-GaAs spectra obtained in Figure 10 and illustrate the narrow range of $\beta_{MQW}(\lambda)$ variations resulting from uncertainties in R_j data.

V. CONCLUSIONS

Photopyroelectric spectroscopy with its inherent sensitivity to low optical absorptions, in combination with optical transmission and reflection FTIR spectroscopes, yielded for the first time quantitative quantum well spectra on SI-GaAs substrates in the sub-bandgap 900–1080 nm region, completely non-destructively. Whereas earlier PPES work on thin films had required the use of an optically transparent substrate material, here $\beta_{Film}(\lambda)$ was calculated *in-situ* even though the substrate was significantly optically absorbing.

A rigorous coupled electromagnetic/thermal-wave theoretical model consisting of a five-layered or a simplified three-layered sample geometry, a photopyroelectric detector, and the PPE signal generation system was developed. The theory was then computer-implemented potentially yielding the calculation of the $\beta(\lambda)$ spectrum of any one of the layers, provided adequate information exists from the total optical reflection and transmission and the thermal-wave response of the system. Furthermore, the substantial influence of thermal contact resistances at the pyroelectric interfaces was examined and interfacial resistance values were calculated. The results showed that little variation in the obtained MQW absorption coefficient values occurs for reasonable values of thermal resistances in fitting the theory to the raw normalized PPE spectra.

The theoretical model further allowed the determination of the origin of optical interferences in the optically opaque region of the MQW due to a buffer GaAs layer between the (Ga,Al)As and substrate Si-GaAs.

APPENDIX

Surface Thermal-Wave Sources in the Geometry of Figure 5

Assuming that at room temperature the non-radiative quantum efficiencies for both thin layers are equal to unity ($\eta_2 = \eta_3 = 1$) the total heat source generated in the absorbing upper two layers may be calculated as follows.

If $\lambda \lesssim 880$ nm the substrate SI-GaAs is optically opaque and hence, the top thin layers will not be affected by light reflected off the back of the substrate. Therefore:

$$A_2 + A_3 = |\hat{T}_{14}|^2(1 - |\hat{R}_{31}|^2 - |\hat{T}_{31}|^2), \tag{A.1}$$

where

$$|\hat{T}_{41}|^2 = \left|\frac{\hat{t}_{12}\hat{T}_{24}e^{-i\hat{k}_2 d_2}}{1 + \hat{r}_{12}\hat{R}_{24}e^{-2i\hat{k}_2 d_2}}\right|^2 \tag{A.2}$$

and

$$|\hat{R}_{24}|^2 = \left|\frac{\hat{r}_{23} + \hat{r}_{34}e^{-2i\hat{k}_3 d_3}}{1 + \hat{r}_{23}\hat{r}_{34}e^{-2i\hat{k}_3 d_3}}\right|^2 \quad \text{and} \quad |\hat{T}_{24}|^2 = \left|\frac{\hat{t}_{23}\hat{t}_{34}e^{-i\hat{k}_3 d_3}}{1 + \hat{r}_{23}\hat{r}_{34}e^{-2i\hat{k}_3 d_3}}\right|^2 \tag{A.3}$$

where the reflectance and transmittance terms, $|\hat{R}_{24}|^2$ and $|\hat{T}_{24}|^2$, are the fraction of energy reflected or transmitted out of layer (3). In general, the expressions for the reflectance and transmittance contain oscillating components; for example:

$$|\hat{R}_{24}|^2 = \frac{|\hat{r}_{23}|^2 + |\hat{r}_{34}|^2 e^{-2\beta_3 d_3} + (2|\hat{r}_{23}||\hat{r}_{34}|e^{-\beta_3 d_3}\cos(\Theta_{23} - \Theta_{34} + \gamma_3 d_3))}{1 + |\hat{r}_{23}|^2|\hat{r}_{34}|^2 e^{-2\beta_3 d_3} + (2|\hat{r}_{23}||\hat{r}_{34}|e^{-\beta_3 d_3}\cos(\Theta_{23} + \Theta_{34} - \gamma_3 d_3))} \tag{A.4}$$

These oscillating terms create interference fringes in the eventual calculation of the PPE voltage; thus, as stated in the main text, an arithmetic average is taken.[20] Equation (A.4) then becomes:

$$|\hat{R}_{24}|^2 = \frac{|\hat{r}_{23}|^2 + |\hat{r}_{34}|^2 e^{-2\beta_3 d_3}}{1 + |\hat{r}_{23}|^2|\hat{r}_{34}|^2 e^{-2\beta_3 d_3}} \tag{A.5}$$

If $\lambda \gtrsim 880$ nm, reflection from the back surface of the substrate may be significant. Therefore:

$$A_2 + A_3 = (1 - |\hat{R}|^2 - |\hat{T}|^2) - A_4 \tag{A.6}$$

where A_4 is the thermal energy created in the substrate layer and $|\hat{R}|^2$ and $|\hat{T}|^2$ are the total reflectance and transmittance of the multilayer sample. These functions are given below upon use of arithmetic averages for the trigonometric dependencies:

$$|\hat{R}|^2 = \left|\frac{\hat{r}_{12} + \hat{R}_{21}e^{-2i\hat{k}_2 d_2}}{1 + \hat{r}_{12}\hat{R}_{21}e^{-2i\hat{k}_2 d_2}}\right|^2 \simeq \frac{|\hat{r}_{12}|^2 + |\hat{R}_{21}|^2 e^{-2\beta_2 d_2}}{1 + |\hat{r}_{12}|^2|\hat{R}_{21}|^2 e^{-2\beta_2 d_2}} \tag{A.7}$$

$$|\hat{T}|^2 = \left|\frac{\hat{t}_{12}\hat{T}_{21}e^{-\hat{k}_2 d_2}}{1 + \hat{r}_{12}\hat{R}_{21}e^{-2i\hat{k}_2 d_2}}\right|^2 \simeq \frac{|\hat{t}_{12}|^2|\hat{T}_{21}|^2 e^{-\beta_2 d_2}}{1 + |\hat{r}_{12}|^2|\hat{R}_{21}|^2 e^{-2\beta_2 d_2}} \tag{A.8}$$

The reflectance and transmittance terms $|\hat{R}_{21}|^2$ and $|\hat{T}_{21}|^2$ are the fractions of energy reflected and transmitted out of both layers (3) and (4):

$$|\hat{R}_{21}|^2 \simeq \frac{|\hat{r}_{23}|^2 + |\hat{R}_{31}|^2 e^{-2\beta_3 d_3}}{1 + |\hat{r}_{23}|^2|\hat{R}_{31}|^2 e^{-2\beta_3 d_3}} \quad \text{and} \quad |\hat{T}_{21}|^2 \simeq \frac{|\hat{t}_{23}|^2|\hat{T}_{31}|^2 e^{-\beta_3, d_3}}{1 + |\hat{r}_{23}|^2|\hat{R}_{31}|^2 e^{-2\beta_3 d_3}}. \tag{A.9}$$

Similarly,

$$|\hat{R}_{31}|^2 \simeq \frac{|\hat{r}_{34}|^2 + |\hat{r}_{41}|^2 e^{-2\beta_4 d_4}}{1 + |\hat{r}_{34}|^2|\hat{r}_{41}|^2 e^{-2\beta_4 d_4}} \quad \text{and} \quad |\hat{T}_{31}|^2 \simeq \frac{|\hat{t}_{34}|^2|\hat{t}_{41}|^2 e^{-\beta_4 d_4}}{1 + |\hat{r}_{34}|^2|\hat{r}_{41}|^2 e^{-2\beta_4 d_4}} \tag{A.10}$$

If the non-radiative quantum efficiencies for the thin layers are not equal, or as in $\eta_{MQW}(\lambda)$ calculations, only η_{MQW} is varied, then we write instead of Equation (A6):

$$A_2 = |\hat{t}_{12}|^2(1 - |\hat{R}_{13}|^2 - |\hat{T}_{13}|^2) \tag{A.11}$$

and

$$A_3 = |\hat{T}_{13}|^2(1 - |\hat{R}_{24}|^2 - |\hat{T}_{24}|^2) \tag{A.12}$$

ACKNOWLEDGEMENT

The support of the Natural Sciences and Engineering Research Council of Canada (NSERC) through a Strategic Grant is gratefully acknowledged.

REFERENCES

1. C. Christofides, A. Mandelis, K. Ghandi and R. E. Wagner, *Rev. Sci. Instrum.*, **61,** 2360 (1990).
2. C. Christofides, A. Engel and A. Mandelis, *Ferroelectrics*, **118,** 411 (1990).
3. A. Mandelis, R. E. Wagner, K. Ghandi and R. Baltman, *Phys. Rev. B.*, **39,** 5254 (1988).
4. C. Christofides, A. Mandelis and A. Engel, *Can J. Phys.*, **69,** 317 (1991).
5. J. Filipowicz, C. Ghezzi and L. Tarricone, *Solid State Commun.*, **74,** 533 (1990).
6. D. A. B. Miller, D. S. Chemla, D. J. Eilenberger, P. W. Smith, A. C. Gossard and W. T. Tsang, *Appl. Phys. Lett.*, **41,** 679 (1982).
7. A. F. S. Penna, J. Shan, A. E. DiGiovanni, A. Y. Cho and A. C. Gossard, *Appl. Phys. Lett.*, **47,** 591 (1985); C. Wetzel, V. Petrova-Koch, M. Zachau, F. Koch and D. Grützmacher, *Superlattices Microstructures*, **6,** 99 (1989).
8. N. Yacoubi, Ph.D. Thesis, Univ. of Montpellier (1986); D. Fournier and A. C. Boccara, in "Photoacoustic and Thermal Wave Phenomena in Semiconductors" (A. Mandelis, Ed., North-Holland, New York, 1987), Chap. 10.3.
9. N. C. Fernelius, *J. Appl. Phys.*, **51,** 650 (1980).
10. G. C. Rune, P. O. Holtz, B. Monemar, M. Sundaram, J. L. Merz and A. C. Gossard, *Superlattices Microstructures*, **7,** 81 (1990).
11. B. Sermage, F. Alexandre, J. Beerens and P. Tronc, *Superlattices Microstructures*, **6,** 373 (1989).
12. O. J. Glembocki, B. V. Shanabrook, N. Bottka, W. T. Beard and J. Comas, *Appl. Phys. Lett.*, **46,** 970 (1985).
13. H. Shen, P. Parayanthal, F. H. Pollack, M. Tomkiewicz, T. J. Drummond and J. N. Schulman, *Appl. Phys. Lett.*, **48,** 653 (1986).
14. C. Christofides, K. Ghandi and A. Mandelis, *Meas. Sci. Technol.*, **1,** 1363 (1990).
15. Kynar™ Piezo Film Technical Manual, Pennwalt Corp., King of Prussia, PA, 1983.
16. A. Petrou, Dept. Physics and Astronomy, State Univ. of New York at Buffalo (private communication); A. F. Terzis, X. C. Liu, A. Petrou, B. D. McCombe, M. Dutta, H. Shen, D. D. Smith, M. W. Cole, M. Taysing-Lara and P. G. Newman, *J. Appl. Phys.*, **67,** 2501 (1990).
17. T. Schurter, Dept. Physics and Astronomy, State University of New York at Buffalo (private communication).
18. S. W. Kirchoefer, N. Holonyak, Jr., K. Hess, D. A. Guilino, H. G. Drickamer, J. J. Coleman and P. D. Dapkus, *Appl. Phys. Lett.*, **40,** 821 (1982).
19. E. H. Putley, in "Semiconductors and Semimetals" (R. K. Willardson and A. C. Beer, Eds., Academic, New York, 1970), Vol. **5,** p. 259.
20. K. Driss-Khodja, A. Gheorghiu and M. L. Theye, *Opt. Commun.*, **55,** 169 (1985).
21. A. Mandelis and M. Zver, *J. Appl. Phys.*, **57,** 4421 (1984).
22. J. S. Blakemore, L. Sargent, R. S. Tang and E. M. Swiggard, *Appl. Phys. Lett.*, **54,** 2106 (1989).
23. J. S. Blakemore, *J. Appl. Phys.*, **53,** R 123 (1982).
24. X. L. Zheng, D. Heiman, B. Law and F. A. Chambers, *Appl. Phys. Lett.*, **52,** 287 (1987).
25. E. Fortin, B. Y. Hua, A. P. Roth, A. Charlebois, S. Fafard and C. Lacelle, *J. Appl. Phys.* **66,** 4854 (1989).
26. A. Othonos, Dept. of Physics, University of Toronto.

27. E. D. Palik in "Handbook of Optical Constants of Solids" (E. D. Palik, Ed., Academic, Orlando, 1985) p. 429.
28. See, for example: K. Wasa, K. Tsubouchi and N. Mikoshiba, *Jpn. J. Appl. Phys.*, **19,** L653 (1980); L. Eaves, H. Vargas and P. J. Williams, *Appl. Phys. Lett.*, **38,** 768 (1981); H. Tokumoto and T. Ishiguro, *Jpn. J. Appl. Phys.*, **22-3** (Supplement), 202 (1983); M. Morita and F. Sato, *Jpn. J. Appl. Phys.*, **22-3** (Supplement), 199 (1983).